Field-Aligned Currents in Auroral Vortices

Jay R. Johnson,[1] Simon Wing,[2] and Peter Delamere,[3]

[1]Andrews University, Berrien Springs, MI, USA.

[2]Johns Hopkins University, Applied Physics Laboratory, Laurel, MD, USA.

[3]Geophysical Institute, University of Alaska, Fairbanks, Alaska, USA.

Abstract. Auroral bright spots have been observed at Earth, Jupiter, and Saturn in regions that map to the boundary layer. It has been suggested that the bright spots are associated with Kelvin-Helmholtz instability. We utilize a quasistatic magnetosphere-ionosphere coupling model driven by a vortex in the boundary layer to determine how the field-aligned current structure depends on ionospheric and boundary layer parameters. We compare vortex induced currents with shear-flow induced currents. We find that the strength of the maximum currents are comparable, but the structure is significantly different. For a vortex, the current and electron precipitation maximize when the vortex size mapped to the ionosphere is approximately 1.5 L, where $L \equiv \sqrt{\Sigma_P/\kappa}$ is the auroral scale length, Σ_P is the Pedersen conductivity, and κ is the Knight parameter. For a vortex, the current width provides a direct measure of the size, Δ, of the boundary layer structure, while shear-flow aurora generally are determined by the larger of Δ or L. For comparison with observations, an event is considered where auroral bright spots in the ionosphere are detected by DMSP SUSSI UVI when Kelvin-Helmholtz structures are observed on the dusk flank by THEMIS.

1. Introduction

Velocity shears in the boundary layer of Earth and other planets have been correlated with auroral arcs and field-aligned currents [*Sonnerup*, 1980; *Lundin and Evans*, 1985]. Free energy from the shear is also known to drive Kelvin-Helmholtz instabilities (KHI) [*Johnson et al.*, 2014] leading to the slow development of Kelvin-Helmholtz vortex structures [*Hasegawa et al.*, 2006, 2009]. Some of the most commonly observed auroral features are folds and vortex-like curls [*Hallinan and Davis*, 1970]. Periodic brights spots have been detected by the UV imager on the Viking spacecraft [*Lui et al.*, 1989; *Potemra et al.*, 1990]. *Lui et al.* [1989] suggested that the bright spots may be associated with Kelvin-Helmholtz instability, which couples to the ionosphere through a field-aligned current system. Figure 1a shows an example of the auroral bead structures detected by the DMSP SSUSI UV instrument when a KH vortex was simultaneously observed at the magnetopause boundary. Recently, the Cassini spacecraft has detected the presence of bright auroral substructures with a characteristic size ranging from 500 km to thousands of km in the noon and dusk sectors [*Grodent et al.*, 2011] as shown in Figure 1b. The fragmentation of the main ring of emission into small-scale spots appears to be associated with structuring of the field-aligned current system based on magnetic field perturbations observed with Cassini/MAG [*Talboys et al.*, 2009a, b, 2011; *Delamere et al.*, 2013]. Such field-aligned currents naturally develop as Kelvin-Helmholtz vortices twist magnetic field lines leading to the suggestion that the vortices result from Kelvin-Helmholtz instability.

The currents and auroral precipitation associated with Kelvin-Helmholtz structures are controlled by the coupling of boundary layer with the ionosphere [*Lyons*, 1980; *Wei and*

Lee, 1993; *Lotko et al.*, 1987; *Echim et al.*, 2007, 2008]. Ionospheric currents are driven by the electric field of the vortex, which maps into the ionosphere. Vortices can drive upward currents in the center of the vortex, and field-aligned potential drops that develop to carry the current can accelerate electrons, which precipitate in the ionosphere. In the case of shear layers, it has been shown that physical properties of the current generator can be inferred from the ionospheric signatures [*Simon Wedlund et al.*, 2013; *Echim et al.*, 2019]. In this paper we examine how the boundary layer and ionospheric parameters control the currents and precipitation, and we examine the differences between vortex driven currents vs shear flow driven currents.

2. Model

Previously, we examined the dependence of shear-driven field-aligned currents on solar wind and ionospheric parameters [*Johnson and Wing*, 2015; *Wing and Johnson*, 2015]. We used a one-dimensional model that specified a velocity field intended to model the interface between a flowing boundary layer plasma and a stagnant magnetospheric plasma. In contrast, in the nonlinear stage of Kelvin-Helmholtz instability, the shear layer is broken up into circulating vortex structures. The slow development of the vortices allows electrons to respond rapidly along the magnetic field setting up a current voltage relationship, which we characterize by a Knight relationship [*Knight*, 1973]. We then follow the procedure outlined in *Johnson and Wing* [2015] to obtain a solution for the field-aligned current density for a specified vortex structure.

Following previous studies [*Lyons*, 1980; *Wei and Lee*, 1993; *Echim et al.*, 2007, 2008; *De Keyser and Echim*, 2013] we solve the equation of current continuity in the ionosphere

$$\nabla \cdot \Sigma_P \nabla \phi_i = j_\parallel(\phi_m, \phi_i) \tag{1}$$

where ϕ_m and ϕ_i are the potential in the magnetosphere and ionosphere respectively. The profile of ϕ_m is specified to capture the basic structure of a Kelvin-Helmholtz vortex. In our model, the potential drop between the magnetosphere and ionosphere drives a parallel current out of the ionosphere determined by a linear Knight relation [*Knight*, 1973]

$$j_\parallel = \kappa(\phi_i - \phi_m), \tag{2}$$

where the Knight conductivity, $\kappa = n_e e^2/\sqrt{2\pi m_e T_e}$, is controlled by the density and temperature of magnetospheric electrons, which carry the upward field-aligned currents. The linear Knight relation is obtained from an expansion of the nonlinear current-voltage relation when $1 \ll e(\phi_i - \phi_m)/T_e \ll b$ ($b = B_i/B_m$ where B_m and B_i are the magnetic field strength at the top and bottom of the potential drop). For simplicity, we will assume that κ is constant throughout the shear layer, recognizing that the current profile will be primarily controlled by the value of density and temperature close to the current maximum.

The assumption of a linear Knight relation is reasonable when the ratio of the potential drop to the average electron thermal energy is smaller than the mirror ratio. This is generally the case at Earth's dayside magnetopause as well as the field-aligned current system associated with the breakdown of corotation at Saturn [*Johnson and Wing*, 2015; *Ray et al.*, 2013]. At Jupiter the potential drop associated with the breakdown of corotation can be large and a full Knight relation may be necessary to describe current

saturation [*Echim et al.*, 2007; *Ray et al.*, 2009]. However, the vorticity associated with Kelvin-Helmholtz vortices is typically weaker than that associated with the large-scale boundary flows due to viscous interaction and mixing, and the linear Knight relation can provide some insights. The solutions obtained for the field-aligned current using the linear Knight relation should always be compared with the saturation current, $nev_{the}b/\sqrt{2\pi}$, to ensure their validity.

In our previous analysis of the shear layer, we found a simple relationship for the dependence of the current density profile on magnetospheric and ionospheric parameters. The main feature of the profile, maximum current density and thickness, are provided in Table 1. Observations of currents detected in the dayside upward region 1 current system are well organized by the theoretical prediction for the maximum current density [*Wing and Johnson*, 2015]. The spatial dependence of the current density on the width of the shear layer Δ is shown in Figure 3. In this case, the currents are driven by potential drop across the shear layer and maximize as the shear increases and width of the boundary layer decreases.

The primary difference between the vortex analysis and previous analysis of shear-driven currents [*Lyons*, 1980; *Echim et al.*, 2008; *Johnson and Wing*, 2015] lies in the specification of the magnetospheric potential, ϕ_m. The velocity field is approximated as a cylindrically symmetric vortex, which captures the essential features of the Kelvin-Helmholtz structure as illustrated in Figure 2

$$\phi_m(\rho_m) = -V_0 B_0 \Delta_m \exp(-\rho_m^2/2\Delta_m^2) \tag{3}$$

with a velocity field

$$V_\varphi(\rho_m) = \frac{\mathbf{B_0} \times d\phi(\rho_m)/d\rho_m}{B_0^2} = V_0 \frac{\rho_m}{\Delta_m} \exp(-\rho_m^2/2\Delta_m^2) \tag{4}$$

where ρ_m is a radial coordinate in the magnetosphere and Δ_m is the characteristic scale of the vortex, where the velocity maximizes. This form of the velocity field dictates that we solve Equation 1 in cylindrical coordinates.

Assuming constant conductivity and combining Equations 1 and 2, we find

$$\frac{1}{\rho_i}\frac{d}{d\rho_i}\rho\frac{d\phi_i}{d\rho_i} = \frac{\phi_i - \phi_m}{L^2} \tag{5}$$

where $L = \sqrt{\Sigma_P/\kappa}$ is the well known electrostatic auroral scale length [*Lyons*, 1980].

In this case, it is useful to employ the azimuthally symmetric Hankel transform

$$\begin{aligned} \Phi(q) &= \int_0^\infty \phi(\rho) J_0(q\rho)\rho d\rho \\ \phi(\rho) &= \int_0^\infty \Phi(q) J_0(q\rho) q dq \end{aligned} \tag{6}$$

Cylindrical symmetry implies that

$$\Phi_i(q) = \left(\frac{1}{1+q^2L^2}\right)\Phi_m(q) \tag{7}$$

$$\Delta\Phi(q) = \Phi_i - \Phi_m = -\left(\frac{q^2L^2}{1+q^2L^2}\right)\Phi_m \tag{8}$$

$$j_\parallel(q) = -\kappa\left(\frac{q^2L^2}{1+q^2L^2}\right)\Phi_m(q) \tag{9}$$

The potential should be expressed in terms of the ionospheric coordinate

$$\phi_m(\rho_i) = -V_0 B_0 \Delta_m \exp(-\rho_i^2/2\Delta_i^2) \tag{10}$$

Performing the Hankel transform in terms of the radial ionospheric coordinate, ρ_i, we obtain

$$\Phi_m(q) = -V_0 B_0 \Delta_m \int_0^\infty e^{-\rho^2/2\Delta_i^2} J_0(q\rho)\rho d\rho = -V_0 B_0 \sqrt{b}\Delta_i^3 e^{-q^2\Delta_i^2/2} \tag{11}$$

where from now on we let $\rho_i = \rho$. The parallel current density is then obtained by the inverse Hankel transform.

$$j_\parallel(\rho) \;=\; \Sigma_P V_0 B_0 \sqrt{b} \Delta_i^3 \int_0^\infty \frac{q^2 e^{-q^2\Delta_i^2/2}}{1+q^2L^2} J_0(q\rho) q dq \tag{12}$$

The maximum value of the current density occurs at the vortex center, $\rho = 0$. Therefore,

$$\begin{aligned} j_{\parallel,\max} \;&=\; \lim_{\rho\to 0} \Sigma_P V_0 B_0 \sqrt{b} \Delta_i^3 \int_0^\infty \frac{q^2 e^{-q^2\Delta_i^2/2}}{1+q^2L^2} J_0(q\rho) q dq \\ &=\; \frac{\Sigma_P V_0 B_0 \sqrt{b} \Delta_i^3}{2L^4} \int_0^\infty \frac{\mu e^{-2\alpha^2\mu}}{1+\mu} d\mu \\ &=\; \kappa V_0 B_0 \Delta_m \left[1 - 2\alpha^2 e^{2\alpha^2} E_1(2\alpha^2)\right] \end{aligned} \tag{13}$$

where $\alpha \equiv \Delta_i/2L$ and

$$E_1(z) = \int_1^\infty \frac{e^{-zt}}{t} dt \tag{14}$$

is the exponential integral.

In the limit $\alpha \ll 1$,

$$E_1(z) = -\gamma - \log(z) + \sum_{k=1}^{\infty} \frac{(-1)^{k+1} z^k}{k k!} \tag{15}$$

$$\begin{aligned} j_{\parallel,\max} \;&=\; \kappa V_0 B_0 \Delta_m \left[1 - 2\alpha^2(1+2\alpha^2+...)(-\gamma - \log(2\alpha^2) + 2\alpha^2 + ...)\right] \\ &=\; \kappa V_0 B_0 \Delta_m (1 + 2\alpha^2 \log(2\alpha^2) + ...) \\ &=\; \kappa V_0 B_0 \Delta_m (1 + \frac{\Delta_i^2}{L^2} \log(\Delta_i/L) + ...) \end{aligned} \tag{16}$$

It should be noted here that the current is much smaller than for a shear layer by a factor $\mathcal{O}(\alpha)$, cf. Table 1.

For $\alpha \gg 1$

$$E_1(z) \sim \frac{e^{-z}}{z}\left[1 - \frac{1}{z} + \frac{2}{z^2} + ...\right] \tag{17}$$

so that

$$
\begin{aligned}
j_{\parallel,\max} &\sim \kappa V_0 B_0 \Delta_m \left[1 - \left(1 - \frac{1}{2\alpha^2} + \frac{1}{2\alpha^4} + ...\right)\right] \\
j_{\parallel,\max} &\sim \kappa V_0 B_0 \Delta_m \left[\frac{1}{2\alpha^2} - \frac{1}{2\alpha^4} + ...\right] \\
j_{\parallel,\max} &\sim 2\frac{\Sigma_P V_0 B_0 b}{\Delta_m}\left[1 - \frac{4L^2}{\Delta_i^2}\right]
\end{aligned} \tag{18}
$$

It should be noted that for large α the maximum current density is enhanced by a factor of 4 relative to the shear layer value.

A uniform approximation [*Bender and Orszag*, 1978] generally valid for all values of α may be found

$$
j_{\parallel,\max} \approx \kappa \frac{V_0 B_0 \Delta_m}{1 + 2\alpha^2} = \frac{2\Sigma_P V_0 B_0 b \Delta_m}{\Delta_m^2 + 2bL^2} \tag{19}
$$

It should be readily apparent that the current density vanishes in either the limit that $\Delta_m \to 0$ or $\Delta_m \to \infty$, and the current density takes on a maximum value at an intermediate value of Δ_m. From Equation 13 it can be found that the maximum current density occurs at $\Delta_i = 1.5L$ and $j_{\parallel,\max} = 0.57\kappa V_0 B_0 L$. This result is in close agreement with that obtained from the uniform approximation (Equation 19) where the maximum current density occurs at $\Delta_i = \sqrt{2}L$ and $j_{\parallel,\max} = \kappa V_0 B_0 L/\sqrt{2}$.

3. Width of the Vortex Current

Performing a Taylor expansion about the maximum current density at $x = 0$, we find

$$
j_\parallel(x) \approx j_{\parallel,\max}\left(1 - \frac{x_i^2}{2\sigma^2}\right) \tag{20}
$$

where

$$
\sigma \equiv \sqrt{\left.\frac{-j_\parallel}{d^2 j_\parallel / dx^2}\right|_{x=0}}. \tag{21}
$$

Taking the second derivative of the current

$$\begin{aligned}
\frac{d^2 j_\parallel}{dx^2} &= \lim_{\rho\to 0} \Sigma_P V_0 B_0 \sqrt{b} \Delta_i^3 \int_0^\infty \frac{q^2 e^{-q^2\Delta_i^2/2}}{1+q^2L^2} \left(\frac{d^2}{d\rho^2} J_0(q\rho)\right) q dq \\
&= \lim_{\rho\to 0} \Sigma_P V_0 B_0 \sqrt{b} \Delta_i^3 \int_0^\infty \frac{q^2 e^{-q^2\Delta_i^2/2}}{1+q^2L^2} \left(\frac{-q^2}{2}(J_0(q\rho) - J_2(q\rho))\right) q dq \\
&= -\frac{\Sigma_P V_0 B_0 \sqrt{b} \Delta_i^3}{4L^6} \int_0^\infty \frac{\mu^2 e^{-2\alpha^2\mu}}{1+\mu} d\mu \\
&= -\kappa \frac{V_0 B_0 \Delta_m}{2L^2} \left[\frac{1}{2\alpha^2} - \left(1 - 2\alpha^2 e^{2\alpha^2} E_1(2\alpha^2)\right)\right] \qquad (22)
\end{aligned}$$

Then for $\alpha \ll 1$

$$\sigma \approx \Delta_i \qquad (23)$$

while for $\alpha \gg 1$

$$\sigma \approx \frac{\Delta_i}{2} \qquad (24)$$

In contrast with the shear layer, the width of the current layer mostly depends on the size of the driver. An estimate for the full width at half maximum (Λ) can be obtained by recognizing that if the current density were fit to a Gaussian of width σ, then $\Lambda = 2\sqrt{2\ln 2}\sigma$.

4. The Spatial Dependence of the Current

Having established the typical strength and width of the current structure associated with a vortex, it is useful to examine the exact solution of Equation 12 obtained from direct integration using standard methods. The results are presented in Figure 3. The parallel current density is shown as a function of x/L in panel (a). In panel (b) the normalized current, $j_\parallel/j_{\parallel,\max}$ is shown. For comparison, panels (c) and (d) show the same variables for a shear layer [*Johnson and Wing*, 2015]. The width of the current layer is obtained directly from panels (b) and (d) as the isocontour where $j_\parallel(\Lambda/2) = j_{\parallel,\max}/2$.

For the vortex, the analytic width for small and large α (Equations 23 and 24) are shown as broken yellow and magenta lines. It is apparent from the isocontour that the width vanishes as $\alpha \to 0$ in panel (b), whereas it reaches a limiting value the order of L in panel (c). This result demonstrates that an auroral vortex structure maps directly the a boundary layer vortex structure, but an auroral feature associated with a velocity shear interface will not map directly if $\Delta_i \lesssim L$.

For the 2008 April 23 09:35-09:43 UT event shown in Figure 1a, we have simultaneous observations of DMSP F16 SSUSI FUV imager [*Paxton et al.*, 1993], SSJ5 particle precipitation [*Hardy et al.*, 1984], magnetic field [*Rich et al.*, 1985], and THEMIS C magnetic field [*Auster et al.*, 2008] and plasma [*McFadden et al.*, 2008] at the Earth's boundary layer. This event has been identified as a Kelvin-Helmholtz event in the survey performed by *Kavosi and Raeder* [2015]. NASA OMNI provides the solar wind data for this event: solar wind speed $V = 580\text{km}\,\text{s}^{-1}$, $n = 5.5\text{cm}^{-3}$, and IMF$(B_x, B_y, B_z) = (4, -8, -5)$nT. The THEMIS C observations within the Kelvin-Helmholtz structures found at the boundary layer provide the electron density and temperature, $n_e = 2\text{cm}^{-3}$ and $T_e = 5$keV, from which we can calculate the Knight κ (see Equation 2). The DMSP F16 trajectory intersects the auroral oval near dusk at 17:30 - 18:00 Magnetlc Local Time (MLT) where the solar zenith angle $\chi \sim 100°$. At this solar zenith angle, the Pedersen conductivity due to the ionizing solar extreme ultraviolet (EUV) radiation is $\Sigma_{p,s} \sim 1S$ [*Ieda et al.*, 2014]. The DMSP SSJ5 observation provides, peak electron energy $E_e = 460$eV, and electron energy flux $\varepsilon = 0.43\,\text{ergs}\,\text{cm}^{-2}\,\text{s}^{-1}\,\text{sr}^{-1}$, from which we obtain Pedersen conductivity due to electron precipitation $\Sigma_{p,e} = 0.1$S using the *Robinson et al.* [1987] formula. The total $\Sigma_p = \sqrt{\Sigma_{p,s}^2 + \Sigma_{p,e}^2} \sim 1S$ [*Wallis and Budzinski*, 1981]. Using these calculated values of

Σ_p and κ, we obtain an auroral electrostatic scale length $L = \sqrt{\Sigma_P/\kappa} = 36$km. From the DMSP magnetic field data or from the size of the bead in the SSUSI image in Figure 1a, we obtain the current width $\Lambda = 126$ km, which would give $\Lambda/L = 3.5$. Table 1 shows that the optimal condition for the maximum current width occurs when and $\Lambda/L = 2.8$, which is very close to the observed value of 3.5.

We can estimate the size of the KH vortex at the magnetopause boundary from the observed value of $\Lambda/L = 3.5$. From the definition of Λ as the FWHM, the current should drop by a factor of 2 at $|x| = \Lambda/2$ or $|x|/L = 1.75$. In Figure 3b, the black curve defines the half-max for a given α and it can be seen that $|x|/L = 1.75$ corresponds to $\alpha \approx 1$. The KH vortex scale mapped to the ionosphere is therefore $\Delta_i = 2\alpha L = 72$km. The KH vortex at the magnetopause boundary $\Delta_m = \sqrt{b}\Delta_i = 3100\text{km} \sim 0.5\text{R}_\text{E}$, where $b = B_i/B_m$, B_m is the magnetic field magnitude at the magnetopause and B_i is the magnetic field magnitude at the ionosphere. Here, we have estimated the values of $B_m = 22$nT and $B_i = 4.1\times10^4$nT from THEMIS and DMSP magnetic field observations, respectively. We note that not all DMSP SSUSI observations for KH events show clear bead structures such as the ones shown in Figure 1a, which may be attributed to non-optimal conditions for obtaining maximum current width and mapping the vortices from the magnetopause boundary to the ionosphere. Figure 4 suggests that electron flux (scaling as $j_\parallel\Delta\phi = j_\parallel^2/\kappa$) is reduced by a factor of 2 outside of the range $0.27 < \alpha < 2$, which corresponds to a range from 800 km to 1 R_E. Structures outside this range would not be distinguishable from the ambient UV emissions in Figure 1a. The conditions favorable to auroral bead structures associated with Kelvin-Helmholtz events will be investigated in our follow up observational study.

At Saturn, the fragmentation of the main ring of emission into small-scale spots shown in (Figure 1b) is suggestive of a similar process. Typical auroral features are localized (500-2000km) auroral bright spots (10-30 kR) that map to the boundary layer. As shown in Figure 4 it is expected that the peak energy flux occurs for scales satisfying $\alpha = 0.75$ and in this regime, the width of the energy flux is $\Lambda_\varepsilon \approx 1.6\Delta_i$. The most prominent scale associated with the bright spots is $\Lambda_\epsilon \approx 2000$ km, which maps to $\Delta_m \approx 1\ R_S$ in the boundary layer (using $\sqrt{B_i/B_m} \sim 60$, and is consistent with the size of K-H structures [*Grodent et al.*, 2011; *Masters et al.*, 2010, 2011]. Using the theory mentioned above, it should be possible to compare the expected auroral intensity vs scale (Δ) to see if the distribution follows the expected trend, and to constrain L (ionospheric conductivity) based on the peak intensity.

5. Discussion and Conclusions

The field-aligned current properties of a shear layer are compared with that of a vortex in Table 1. In the limit that $\Delta_i \gg L$ the maximum current density has essentially the same behavior for shear layers and vortices and the current width scales with Δ_i. The primary difference is in the limit $\Delta_i \ll L$. In this case, the shear layer becomes a discontinuity, but the current in the shear layer spreads out to the auroral scale, L and the current maximizes at $j_{\parallel,\max} = \kappa V_0 B_0 L\sqrt{b}$. On the other hand, the vortex current does not broaden and the current is confined in the vortex structure. As the width of the vortex vanishes, $\Delta \to 0$, the current scales with $j_{\parallel,\max} = \kappa V_0 B_0 \Delta_m$, and also vanishes. For the vortex, the maximum current occurs when $\Delta_i = 1.5L$ and $j_{\parallel,\max} = 0.57\kappa V_0 B_0 L$. For this scale of driver, the current width will be $\Lambda = 2.8L$ and the width of the electron energy flux, $\Lambda_\varepsilon = 2.4L$.

Two important conclusions can be drawn. First, if vortex structures are detected at the ionosphere, they basically map to structure in the boundary layer whereas shear layers only map if the scale is large enough. Secondly, the current density maximizes when the vortex size maps to the auroral scale length with roughly the same strength of current density as for the shear layer. As vortices become either larger or smaller than the optimal size, the current vanishes. This property suggests that it may be useful to obtain the statistics of spot size vs intensity from auroral images in planetary magnetospheres from which it may be possible to infer ionospheric properties knowing that currents maximize when the width is 1.5 L.

Acknowledgments.

The Air Force Research Laboratory and the World Data Center provided the DMSP SSJ4/SSJ5 and MAG data. The DMSP data are available online at a JHU/APL website http://sd-www.jhuapl.edu/Aurora/spectrogram/index.html. The DMSP SSJ4/SSJ5 and MAG data are also available at NASA CDAWeb https://cdaweb.gsfc.nasa.gov/index.html/, at a Boston College website https://dmsp.bc.edu/, and at a NOAA website https://satdat.ngdc.noaa.gov/dmsp/. DMSP SSUSI data are available at a JHU/APL website https://ssusi.jhuapl.edu/. THEMIS data are available at a UC Berkeley website http://themis.ssl.berkeley.edu/index.shtml. Simon Wing acknowledges the support from NASA Grants (NNX15AJ01G, NNX16AQ87G, 80NSSC20K0704, 80NSSC19K0843, 80NSSC19K0822, and 80NSSC20K0188). Work at Andrews University is supported by NASA grants NNX15AJ01G, NNH15AB17I, NNX16AQ87G, 80NSSC19K0270, 80NSSC19K0843, 80NSSC18K0835, 80NSSC20K0355, NNX17AI50G,

235 NNX17AI47G, 80HQTR18T0066, 80NSSC20K0704 and NSF grants AGS1832207 and
236 AGS1602855 and Andrews University FRG 201119.

References

237 Auster, H. U., K. H. Glassmeier, W. Magnes, O. Aydogar, W. Baumjohann, D. Constan-
238 tinescu, D. Fischer, K. H. Fornacon, E. Georgescu, P. Harvey, O. Hillenmaier, R. Kroth,
239 M. Ludlam, Y. Narita, R. Nakamura, K. Okrafka, F. Plaschke, I. Richter, H. Schwarzl,
240 B. Stoll, A. Valavanoglou, and M. Wiedemann (2008), The themis fluxgate magnetome-
241 ter, *Space Science Reviews*, *141*(1-4), 235–264, doi:10.1007/s11214-008-9365-9.

242 Bender, C. M., and S. A. Orszag (1978), *Advanced Mathematical Methods for Scientists*
243 *and Engineers*, Springer.

244 De Keyser, J., and M. Echim (2013), Electric potential differences across auroral generator
245 interfaces, *Annales Geophysicae*, *31*, 251–261, doi:10.5194/angeo-31-251-2013.

246 Delamere, P. A., R. J. Wilson, S. Eriksson, and F. Bagenal (2013), Magnetic signatures
247 of Kelvin-Helmholtz vortices on Saturn's magnetopause: Global survey, *Journal of*
248 *Geophysical Research (Space Physics)*, *118*, 393–404, doi:10.1029/2012JA018197.

249 Echim, M. M., M. Roth, and J. de Keyser (2007), Sheared magnetospheric plasma flows
250 and discrete auroral arcs: a quasi-static coupling model, *Annales Geophysicae*, *25*, 317–
251 330, doi:10.5194/angeo-25-317-2007.

252 Echim, M. M., M. Roth, and J. de Keyser (2008), Ionospheric feedback effects on the
253 quasi-stationary coupling between LLBL and postnoon/evening discrete auroral arcs,
254 *Annales Geophysicae*, *26*, 913–928, doi:10.5194/angeo-26-913-2008.

Echim, M. M., H. Lamy, J. De Keyser, R. Maggiolo, H. Gunell, and C. L. Simon Wedlund (2019), A method to estimate the physical properties of magnetospheric generators from observations of quiet discrete auroral arcs, *Journal of Geophysical Research (Space Physics)*, *124*(12), 10,283–10,293, doi:10.1029/2019JA026969.

Grodent, D., J. Gustin, J.-C. Gérard, A. Radioti, B. Bonfond, and W. R. Pryor (2011), Small-scale structures in Saturn's ultraviolet aurora, *Journal of Geophysical Research (Space Physics)*, *116*, 9225, doi:10.1029/2011JA016818.

Hallinan, T. J., and T. N. Davis (1970), Small-scale auroral arc distortions, *Planetary and Space Science*, *18*, 1735–1735, doi:10.1016/0032-0633(70)90007-3.

Hardy, D. A., L. K. Schmitt, M. S. Gussenhoven, F. J. Marshall, H. Yeh, T. L. Shumaker, A. Hube, and J. Pantazis (1984), Precipitating Electron and Ion Detectors (SSJ/4) for the Block 5D/Flights 6-10 DMSP Satellites: Calibration and Data Presentation, *Rep. AFGL-TR-84-0317, Air Force Geophys. Lab., Hanscom Air Force Base, Mass.*

Hasegawa, H., M. Fujimoto, K. Takagi, Y. Saito, T. Mukai, and H. RèMe (2006), Single-spacecraft detection of rolled-up Kelvin-Helmholtz vortices at the flank magnetopause, *Journal of Geophysical Research (Space Physics)*, *111*, A09203, doi:10.1029/2006JA011728.

Hasegawa, H., A. Retinò, A. Vaivads, Y. Khotyaintsev, M. André, T. K. M. Nakamura, W.-L. Teh, B. U. Ö. Sonnerup, S. J. Schwartz, Y. Seki, M. Fujimoto, Y. Saito, H. Rème, and P. Canu (2009), Kelvin-Helmholtz waves at the Earth's magnetopause: Multiscale development and associated reconnection, *Journal of Geophysical Research (Space Physics)*, *114*, A12207, doi:10.1029/2009JA014042.

277 Ieda, A., S. Oyama, H. Vanhamäki, R. Fujii, A. Nakamizo, O. Amm, T. Hori, M. Takeda,
278 G. Ueno, A. Yoshikawa, R. J. Redmon, W. F. Denig, Y. Kamide, and N. Nishitani
279 (2014), Approximate forms of daytime ionospheric conductance, *Journal of Geophysical*
280 *Research (Space Physics)*, *119*(12), 10,397–10,415, doi:10.1002/2014JA020665.

281 Johnson, J. R., and S. Wing (2015), The dependence of the strength and thickness of
282 field-aligned currents on solar wind and ionospheric parameters, *Journal of Geophysical*
283 *Research (Space Physics)*, *120*, 3987–4008, doi:10.1002/2014JA020312.

284 Johnson, J. R., S. Wing, and P. A. Delamere (2014), Kelvin Helmholtz Instability in
285 Planetary Magnetospheres, *Space Science Review*, *184*, 1–31, doi:10.1007/s11214-014-
286 0085-z.

287 Kavosi, S., and J. Raeder (2015), Ubiquity of kelvin-helmholtz waves at earth's magne-
288 topause, *Nature Communications*, *6*, 7019, doi:10.1038/ncomms8019.

289 Knight, S. (1973), Parallel electric fields, *Planet*, *21*, 741–750.

290 Lotko, W., B. U. O. Sonnerup, and R. L. Lysak (1987), Nonsteady boundary layer flow
291 including ionospheric drag and parallel electric fields, *J. Geophys. Res.,* , *92*, 8635–8648,
292 doi:10.1029/JA092iA08p08635.

293 Lui, A. T. Y., D. Venkatesan, and J. S. Murphree (1989), Auroral bright
294 spots on the dayside oval, *Journal of Geophysical Research*, *94*, 5515–5522, doi:
295 10.1029/JA094iA05p05515.

296 Lundin, R., and D. S. Evans (1985), Boundary layer plasmas as a source for high-latitude,
297 early afternoon, auroral arcs, *Planet. Space Sci.*, *33*, 1389–1406, doi:10.1016/0032-
298 0633(85)90115-1.

Lyons, L. R. (1980), Generation of large-scale regions of auroral currents, electric potentials, and precipitation by the divergence of the convection electric field, *J. Geophys. Res.*, *85*, 17–24, doi:10.1029/JA085iA01p00017.

Masters, A., N. Achilleos, M. G. Kivelson, N. Sergis, M. K. Dougherty, M. F. Thomsen, C. S. Arridge, S. M. Krimigis, H. J. McAndrews, S. J. Kanani, N. Krupp, and A. J. Coates (2010), Cassini observations of a kelvin-helmholtz vortex in saturn's outer magnetosphere, *Journal of Geophysical Research (Space Physics)*, *115*(A7), A07225, doi:10.1029/2010JA015351.

Masters, A., D. Mitchell, A. Coates, and M. Dougherty (2011), Saturn's low-latitude boundary layer: 1. properties and variability, *Journal of Geophysical Research: Space Physics*, *116*(A6).

McFadden, J. P., C. W. Carlson, D. Larson, M. Ludlam, R. Abiad, B. Elliott, P. Turin, M. Marckwordt, and V. Angelopoulos (2008), The themis esa plasma instrument and in-flight calibration, *Space Science Review*, *141*(1–4), 277–302, doi:10.1007/s11214-008-9440-2.

Paxton, L. J., C.-I. Meng, G. H. Fountain, B. S. Ogorzalek, E. H. Darlington, S. A. Gary, J. O. Goldsten, D. Y. Kusnierkiewicz, S. C. Lee, and L. A. Linstrom (1993), Ssusi: horizon-to-horizon and limb-viewing spectrographic imager for remote sensing of environmental parameters, in *Proceedings of the Meeting, 2021 July 1992*, *Society of Photo-Optical Instrumentation Engineers (SPIE) Conference Series*, vol. 1764, edited by R. E. Huffman, pp. 161–176, San Diego, doi:10.1117/12.140846.

Potemra, T. A., R. E. Erlandson, H. Vo, D. Venkatesan, and L. L. Cogger (1990), Periodic auroral forms and geomagnetic field oscillations in the 1400 MLT region, *Journal of*

Geophysical Research, *95*, 5835–5844, doi:10.1029/JA095iA05p05835.

Ray, L. C., Y. J. Su, R. E. Ergun, P. A. Delamere, and F. Bagenal (2009), Current-voltage relation of a centrifugally confined plasma, *Journal of Geophysical Research (Space Physics)*, *114*(A4), A04214, doi:10.1029/2008JA013969.

Ray, L. C., M. Galand, P. A. Delamere, and B. L. Fleshman (2013), Current-voltage relation for the Saturnian system, *Journal of Geophysical Research (Space Physics)*, *118*, 3214–3222, doi:10.1002/jgra.50330.

Rich, F. J., D. A. Hardy, and M. S. Gussenhoven (1985), Enhanced ionosphere-magnetosphere data from the DMSP satellites,, *EOS*, *66*, 513.

Robinson, R. M., R. R. Vondrak, K. Miller, T. Dabbs, and D. Hardy (1987), On calculating ionospheric conductances from the flux and energy of precipitating electrons, *J. Geophys. Res.*, *92*, 2565–2569, doi:10.1029/JA092iA03p02565.

Simon Wedlund, C., H. Lamy, B. Gustavsson, T. Sergienko, and U. Brändström (2013), Estimating energy spectra of electron precipitation above auroral arcs from ground-based observations with radar and optics, *Journal of Geophysical Research (Space Physics)*, *118*, 3672–3691, doi:10.1002/jgra.50347.

Sonnerup, B. U. O. (1980), Theory of the low-latitude boundary layer, *J. Geophys. Res.*, *85*, 2017–2026, doi:10.1029/JA085iA05p02017.

Talboys, D. L., C. S. Arridge, E. J. Bunce, A. J. Coates, S. W. H. Cowley, M. K. Dougherty, and K. K. Khurana (2009a), Signatures of field-aligned currents in Saturn's nightside magnetosphere, *Geophys. Res. Lett.,* , *36*, L19107, doi:10.1029/2009GL039867.

Talboys, D. L., C. S. Arridge, E. J. Bunce, A. J. Coates, S. W. H. Cowley, and M. K. Dougherty (2009b), Characterization of auroral current systems in Saturn's magne-

tosphere: High-latitude Cassini observations, *Journal of Geophysical Research (Space Physics)*, *114*, A06220, doi:10.1029/2008JA013846.

Talboys, D. L., E. J. Bunce, S. W. H. Cowley, C. S. Arridge, A. J. Coates, and M. K. Dougherty (2011), Statistical characteristics of field-aligned currents in Saturn's nightside magnetosphere, *Journal of Geophysical Research (Space Physics)*, *116*, A04213, doi:10.1029/2010JA016102.

Wallis, D. D., and E. E. Budzinski (1981), Empirical models of height integrated conductivities, *Journal of Geophysical Research*, *86*(A1), 125, doi:10.1029/ja086ia01p00125.

Wei, C. Q., and L. C. Lee (1993), Coupling of magnetopause-boundary layer to the polar ionosphere, *Journal of Geophysical Research*, *98*, 5707–5725, doi:10.1029/92JA02232.

Wing, S., and J. R. Johnson (2015), Theory and observations of upward field-aligned currents at the magnetopause boundary layer, *Geophys. Res. Lett.,* , *42*, 9149–9155, doi:10.1002/2015GL065464.

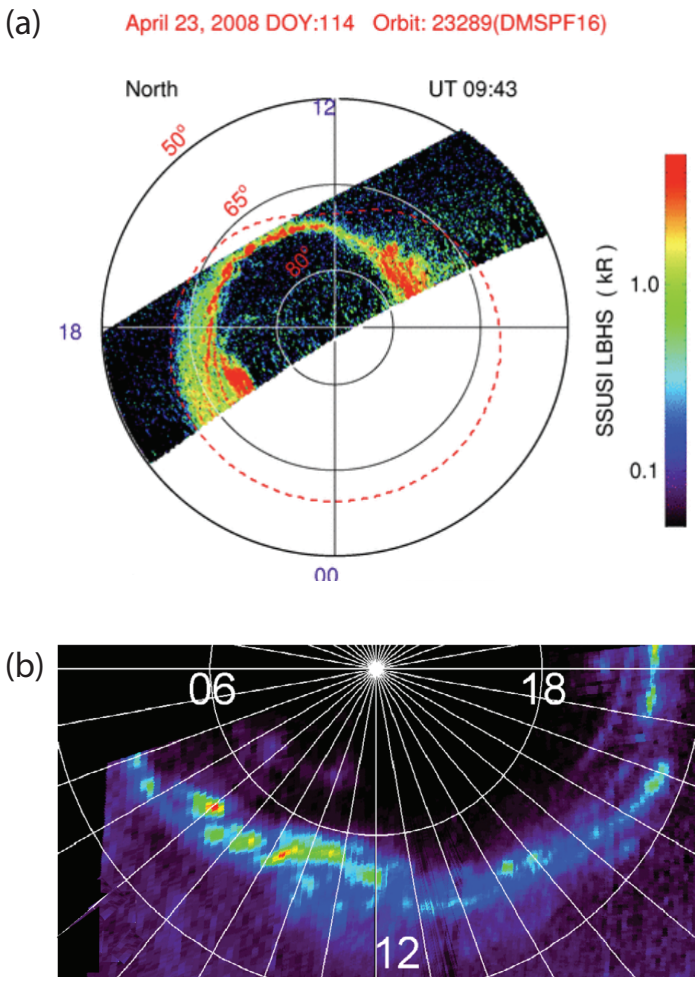

Figure 1. (a) DMSP SSUSI UV image showing auroral bead structure at 13-18 MLT when Kelvin-Helmhotz vortex was simultaneously observed at the magnetopause boundary on the dusk flank by THEMIS B on 2008 April 23 09:35-09:43 UT. (b) A compilation of three polar views of the northern auroral emission at Saturn obtained with the FUV channel of the Cassini-UVIS spectro-imager on August 26, 2008. The image provides a global view of auroral structures obtained over 77 minutes with a spatial resolution of 200 km (adapted from Figure 1 of [*Grodent et al.*, 2011]). A key feature is the cluster of grapes structures, which vary in size and intensity. These structures are thought to be associated with Kelvin-Helmholtz vortices.

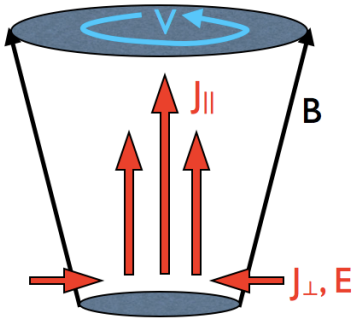

Figure 2. The model includes a driver in the magnetosphere associated with a velocity vortex. The converging electric field of the slowly evolving vortex maps to the ionosphere where it drives Pedersen currents, which are diverted along the magnetic field within the vortex. For simplicity, the vortex is taken to be a cylindrically symmetric velocity ring of characteristic size Δ_m.

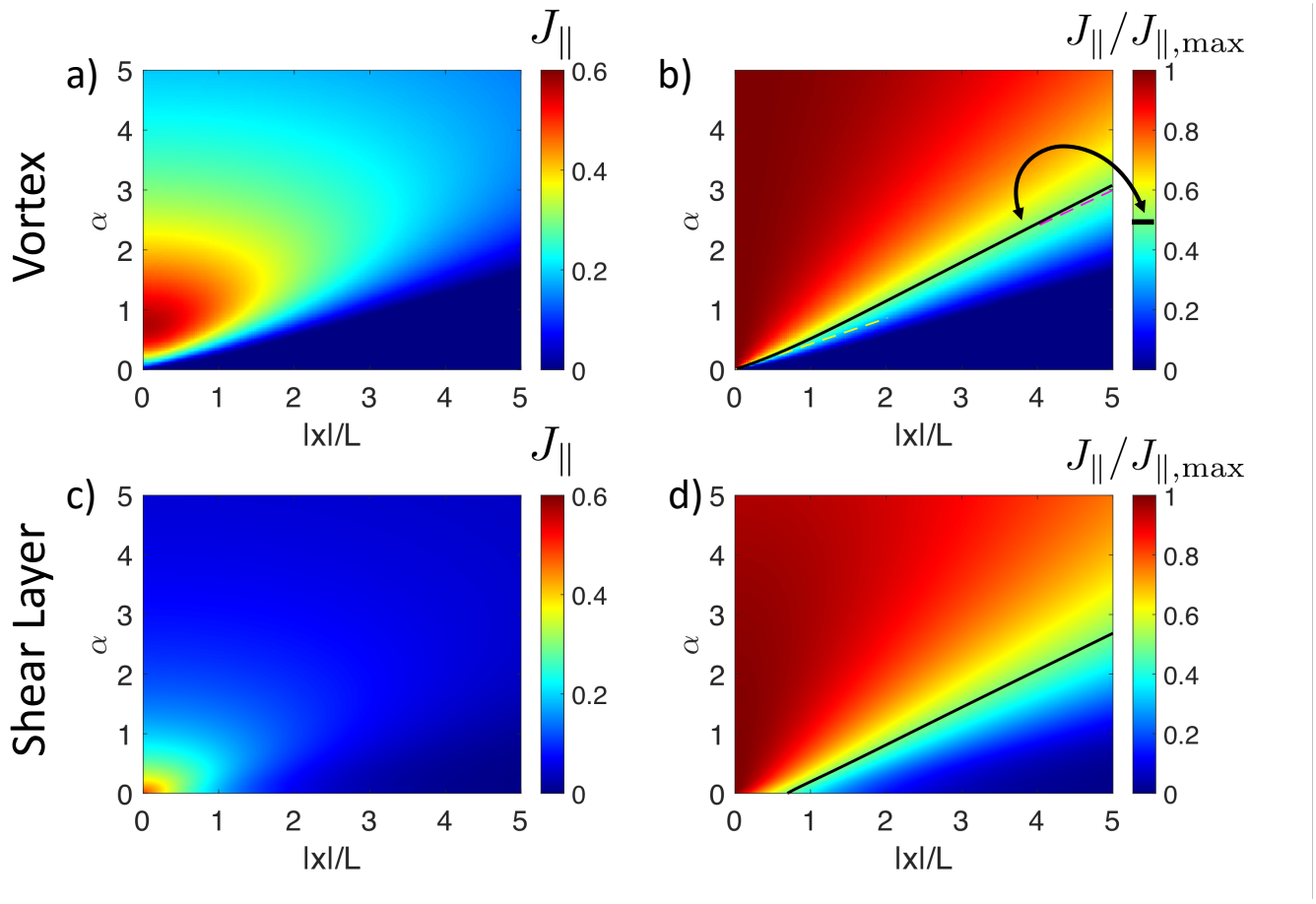

Figure 3. The spatial profile of the current density as a function of x/L for different values of $\alpha = \Delta_i/2L$. Panels (a) and (b) show the current density and normalized current density for the vortex solution. Panels (c) and (d) show current density and normalized current density for the shear-layer solution. The black line on figures (b) and (d) show the half width of the current density for the vortex solution. The yellow and magenta dashed lines show the width based on Equations 23 and 24.

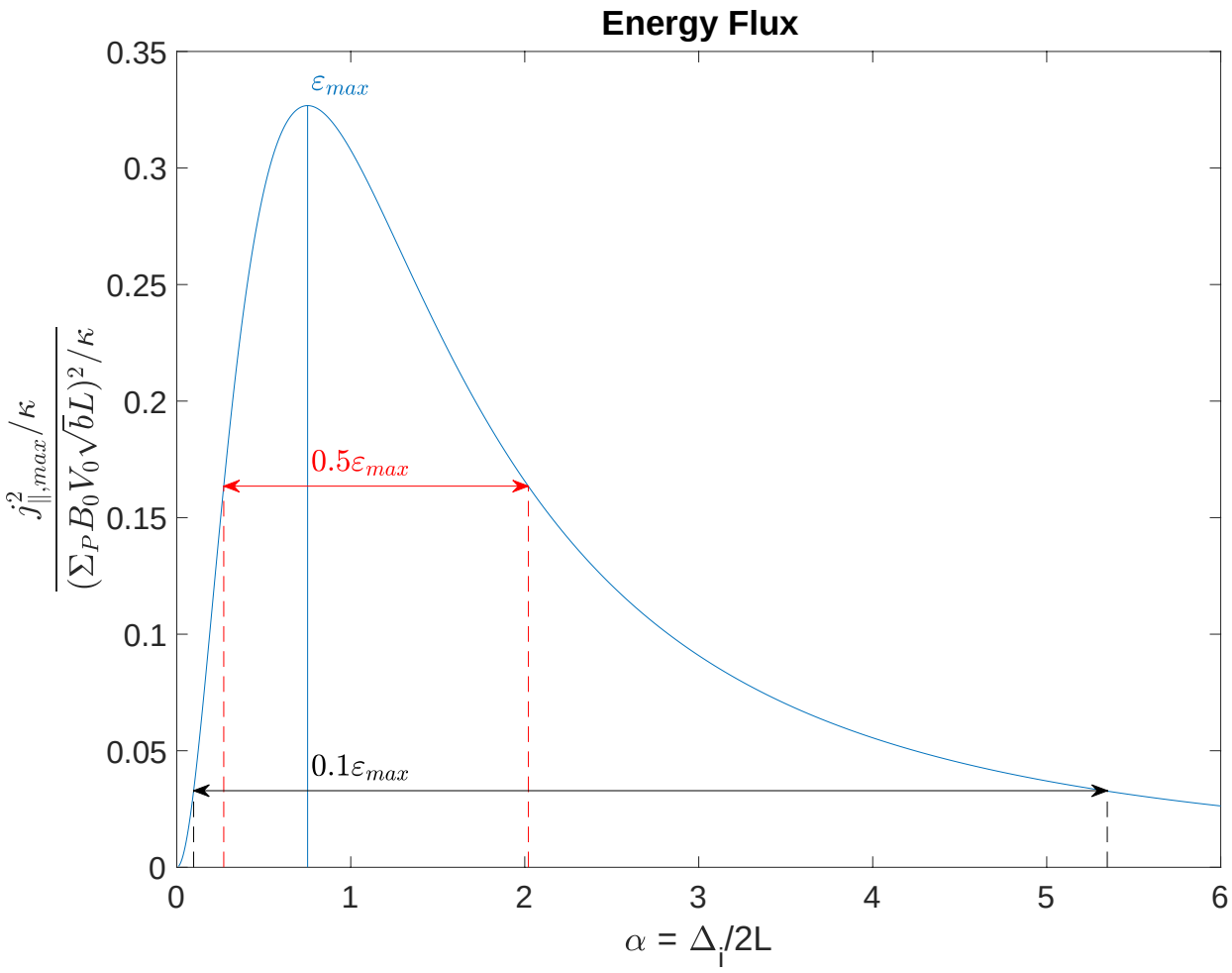

Figure 4. Maximum energy flux ($j_{\parallel}^2/\kappa$) vs scale of the vortex ($\alpha = \Delta_i/2L$), mapped to the ionosphere based on Equation 13. The energy flux peaks at $\alpha = 0.75$. The flux drops by a factor of 2 outside the range $0.27 < \alpha < 2$, and the energy flux drops by a factor of 10 outside the range $0.1 < \alpha < 5.35$. For the event shown in Figure 1, we can infer that $\alpha \approx 1$, which is very close to the optimum size that maximizes the current and energy flux.

Table 1. Comparison of Vortex and Shear Currents

	Vortex	Shear Layer
$j_{\parallel,\max}$	$\frac{2\Sigma_P V_0 B_0 b}{\Delta_m + 2bL^2/\Delta_m}$	$\frac{\Sigma_P V_0 B_0 b}{\Delta_m + \sqrt{b}L}$
$\Lambda(\Delta_i \ll 2L)$	$2.35\Delta_i$	$1.38L$
$\Lambda(\Delta_i \gg 2L)$	$1.67\Delta_i$	$1.76\Delta_i$
$\max_{\Delta}(j_{\parallel,\max})$	$0.57\kappa V_0 B_0 \sqrt{b}L$	$\kappa V_0 B_0 \sqrt{b}L$
$\Delta_i \left(\max_{\Delta}(j_{\parallel,\max})\right)$	$1.5L$	0
$\Lambda \left(\max_{\Delta}(j_{\parallel,\max})\right)$	$2.8L$	$1.38L$